Monthly Notices of the ROYAL ASTRONOMICAL SOCIETY

MNRAS **501,** 6156–6167 (2021) doi:10.1093/mnras/staa3820
Advance Access publication 2020 December 11

H α fluxes and extinction distances for planetary nebulae in the IPHAS survey of the northern galactic plane

Thavisha E. Dharmawardena [1,2,3,4] M. J. Barlow [2★] J. E. Drew [2] A. Seales,[2,5] S. E. Sale [6] D. Jones [7,8] A. Mampaso,[7,8] Q. A. Parker [9,10] L. Sabin [11] and R. Wesson[2]

[1]*Max Planck Institute for Astronomy, Königstuhl 17, D-69117 Heidelberg, Germany*
[2]*Department of Physics and Astronomy, University College London, Gower Street, London WC1E 6BT, UK*
[3]*Academia Sinica Institute of Astronomy and Astrophysics, 11F ASMAB, No.1, Section 4, Roosevelt Rd, Taipei 10617, Taiwan*
[4]*National Central University, No. 300, Zhongda Rd., Zhongli District, Taoyuan City 32001, Taiwan*
[5]*The Royal Institution of Great Britain, 21 Albemarle Street, London W1S 4BS, UK*
[6]*Rudolf Peierls Centre for Theoretical Physics, Keble Road, Oxford OX1 3NP, UK*
[7]*Instituto de Astrofísica de Canarias, E-38205 La Laguna, Tenerife, Spain*
[8]*Departamento de Astrofísica, Universidad de La Laguna, E-38206 La Laguna, Tenerife, Spain*
[9]*Department of Physics, University of Hong Kong, CYM Physics Building, Hong Kong*
[10]*The Laboratory for Space Research, University of Hong Kong, Hong Kong*
[11]*Instituto de Astronomía, Universidad Nacional Autónoma de México, Apdo. Postal 877, C.P. 22860 Ensenada, B.C., México*

Accepted 2020 December 1. Received 2020 December 1; in original form 2020 August 10

ABSTRACT

We report H α filter photometry for 197 Northern hemisphere planetary nebulae (PNe) obtained using imaging data from the IPHAS survey. H α+[N II] fluxes were measured for 46 confirmed or possible PNe discovered by the IPHAS survey and for 151 previously catalogued PNe that fell within the area of the northern Galactic Plane surveyed by IPHAS. After correcting for [N II] emission admitted by the IPHAS H α filter, the resulting H α fluxes were combined with published radio free–free fluxes and H β fluxes, in order to estimate mean optical extinctions to 143 PNe using ratios involving their integrated Balmer line fluxes and their extinction-free radio fluxes. Distances to the PNe were then estimated using three different 3D interstellar dust extinction mapping methods, including the IPHAS-based H-MEAD algorithm of Sale (2014). These methods were used to plot dust extinction versus distance relationships for the lines of sight to the PNe; the intercepts with the derived dust optical extinctions allowed distances to the PNe to be inferred. For 17 of the PNe in our sample reliable *Gaia* DR2 distances were available and these have been compared with the distances derived using three different extinction mapping algorithms as well as with distances from the nebular radius versus H α surface brightness relation of Frew et al. (2016). That relation and the H-MEAD extinction mapping algorithm yielded the closest agreement with the *Gaia* DR2 distances.

Key words: dust, extinction – planetary nebulae: general – planetary nebulae: individual.

1 INTRODUCTION

Accurate distance estimation to Galactic planetary nebulae has represented a persistent difficulty over the years, with many different methods, both direct and statistical, having been applied – see Frew, Parker & Bojičić (2016) for a recent comprehensive summary of the various methods. Although *Gaia* has now measured parallaxes for a significant number of PN central stars (e.g. Kimeswenger & Barría 2018; González-Santamaría et al. 2019), for many PNe high nebular surface brightnesses or faint central star magnitudes make reliable *Gaia* parallaxes difficult to determine. For such nebulae alternative distance estimation methods must be sought.

The Galactic PN distance estimation method that will be discussed in this paper is based on the determination of interstellar dust extinctions and distances to a sufficient number of field stars nearby on the sky to a PN that a plot of the stellar dust extinctions versus distance allows the distance to the PN to be inferred from its measured dust extinction. Early examples of the use of this technique for PN distance estimation were published by Lutz (1973), Kaler & Lutz (1985), and Gathier, Pottasch & Pel (1986). In recent years a number of deep optical and infrared imaging surveys have enabled the production of extensive 3D reddening maps of the Galactic plane, allowing distances to be estimated to stars and nebulae by plotting reddening versus distance for their sightlines (e.g. Marshall et al. 2006; Sale et al. 2009, 2014; Sale 2012; Lallement et al. 2014, 2019; Green et al. 2015, 2019).

The Isaac Newton Telescope Photometric H-alpha Survey of the northern Galactic plane (IPHAS; Drew et al. 2005; Barentsen et al. 2014), in addition to obtaining filter photometry in the Sloan r' and i' bands, has produced a large narrow-band H α photometric sample, enabling many emission line stars and nebulae to be identified and measured. Data from IPHAS have been used to identify new examples of young stellar objects (Vink et al. 2008), classical Be

★ E-mail: mjb@star.ucl.ac.uk

stars Raddi et al. (2015), supernova remnants (Sabin et al. 2013), and planetary nebulae (Mampaso et al. 2006; Viironen et al. 2009a; Corradi et al. 2011; Sabin et al. 2014).

From the initial IPHAS data release (González-Solares et al. 2008) to the second data release (Barentsen et al. 2014) the applications of IPHAS data have expanded. Sale et al. (2009), Sale (2012), and Sale et al. (2014) have demonstrated how the information from colours using the r', i', and (in particular) H α filters enables spectral types and interstellar dust extinctions to be inferred for objects in the IPHAS survey, enabling 3D extinction mapping to be carried out for sightlines covered by the survey. For example, Giammanco et al. (2011) applied the IPHAS-based extinction mapping technique MEAD (Mapping Extinction Against Distance; Sale et al. 2009) to planetary nebulae, using spectroscopic Balmer-line ratios to estimate reddenings and distances for 70 planetary nebulae.

In the past, dust extinctions to PNe have often been obtained from the ratio of radio free–free fluxes (unaffected by dust extinction) to H β filter fluxes. In this paper we measure H α fluxes for a sample of 197 PNe in the northern Galactic Plane observed by IPHAS and use them, along with published integrated H β fluxes that are available for 37 of the nebulae, to determine interstellar dust extinctions to the nebulae. In Section 2 of the paper we present H α flux measurements for 197 PNe observed by IPHAS and correct for the [N II] 6548, 6583 Å contributions to these fluxes. In Section 3 we combine the [N II]-corrected H α fluxes with published H β and radio free–free fluxes in order to derive interstellar dust extinctions to 143 PNe. In Section 4 we derive extinction distances to these PNe using a number of 3D extinction mapping techniques and for 17 PNe in the sample that are judged to have reliable *Gaia* DR2 distances we compare these to the extinction mapping distances.

2 NEBULAR H α FLUXES FOR NORTHERN PLANETARY NEBULAE

2.1 The IPHAS survey

The IPHAS survey (Drew et al. 2005) was carried out using the Wide Field Camera (WFC) on the 2.5 m Isaac Newton telescope located in the Observatorio del Roque de los Muchachos on the island of La Palma. It was a digital optical photometric survey of the northern Galactic plane, carried out in three bands, r', i', and H α. The IPHAS footprint extends over $-5^\circ < b < +5^\circ$ and $30^\circ < l < 215^\circ$, forming an area of approximately 1800 deg^2 (Drew et al. 2005; Barentsen et al. 2014).

The survey obtained images using the WFC's H α narrow-band filter with a full-width at half-maximum (FWHM) bandwidth of 95 Å centred at 6568 Å and broad-band Sloan r' (bandwidth 1380 Å centred at 6260 Å) and i' (bandwidth 1535 Å centred at 7670 Å) filters. Images were taken sequentially with all three filters at each pointing, with exposure times of 120 s for the H α filter and mostly 30 s and 10 s for the r' and i' filters, respectively. The WFC detector pixels projected to 0.333 arcsec per pixel on the sky.

Each WFC image is a mosaic from its four CCDs, capturing a sky area of approximately 0.25 deg^2. To fill in the gaps between the CCDs, a set of offset pointings with the same filters and exposure times was obtained after each prime pointing, resulting in 7635 pairs of telescope pointings being used to capture the total IPHAS survey area (Drew et al. 2005; Barentsen et al. 2014).

The second IPHAS Data Release (DR2) was made available in 2014 (Barentsen et al. 2014). At this time the survey had achieved 5σ magnitude limits of 21.2 $\pm$ 0.5 in the r' band, 20.0 $\pm$ 0.3 in the i' band, and 20.3 $\pm$ 0.03 in the H α band and had covered >90 per cent of the 1800 deg^2 footprint of the IPHAS survey.

2.2 Planetary nebula source selection

The IPHAS survey observed a large number of PNe and PN candidates. We have utilized the Hong Kong/AAO/Strasbourg H α data base[1] (HASH; Parker, Bojičić & Frew 2016) to select nebulae classified as true, likely, or possible PNe from the following sources:

(i) Viironen et al. (2009a): A list of candidate compact PNe from the IPHAS survey, of which we measured four that are listed in the HASH data base as true or possible PNe.

(ii) Sabin et al. (2014): A catalogue of IPHAS-discovered potential PNe based on the spectroscopic and morphological characteristics of the nebulae (for PN classification criteria see Frew & Parker 2010). We measured 42 of these objects that are listed as true, likely, or possible PNe by the HASH data base, including five objects from the bow-shock nebula discovery paper of Sabin et al. (2010).

(iii) We measured 151 PNe from the Strasbourg-ESO Catalogue (Acker et al. 1992) that had been observed by IPHAS and which are listed as true PNe by the HASH data base.

2.3 H α aperture photometry measurements of PNe observed by IPHAS

The reduced IPHAS H α images are available for download via the INT WFC Archive's Data Quality Control (DQC) query page, hosted by the Cambridge Astronomy Survey Unit (CASU).[2] All sources had multiple observations and all the observations for each source were downloaded, apart from those flagged as having problems. Column 3 of Tables A1 and A2 of Appendix A (see Suppl. material) lists the estimated angular dimensions of the nebulae. For nebulae less than ~5 arcsec in diameter this was measured as their FWHM in the IPHAS H α filter images, then corrected in quadrature by the FWHM of nearby stars of similar brightness. For larger nebulae, the quoted angular dimensions were measured at 10 per cent of the peak nebular brightnesses in the IPHAS H α filter images.

In order to obtain integrated source counts, aperture photometry was carried out using the Caltech Aperture Photometry Tool (APT)[3] and the Starlink Graphical Astronomy and Image Analysis Tool (*GAIA*).[4] The shape (circular/elliptical) and size of the APT aperture used for each PN was adjusted to best match the shape of the PN, as was the annular sky aperture, and the median sky-subtracted net source counts measured. For a small number of PNe in crowded fields for which there were bright stars within the PN aperture, we aimed to include similarly bright stars in the annular sky aperture in order to remove to first order the contribution from the contaminants. We utilized *GAIA* for those nebulae whose angular radii were too large to fit within the APT's radius limit of 200 pixels. For a few very extended low surface brightness nebulae, the IPHAS 120 s H α exposures might not detect the full extent of their emission.

The source counts per second, obtained by dividing the net source counts by the observation exposure times, were converted to instrumental magnitudes and then to filter magnitudes by adding the zero-point filter magnitudes provided for each WFCAM exposure.

[1] http://202.189.117.101:8999/gpne/dbMainPage.php
[2] http://apm3.ast.cam.ac.uk/cgi-bin/wfs/dqc.cgi
[3] http://www.aperturephotometry.org/aptool/
[4] http://www.starlink.rl.ac.uk/star/docs/sun214.htx/sun214.html/

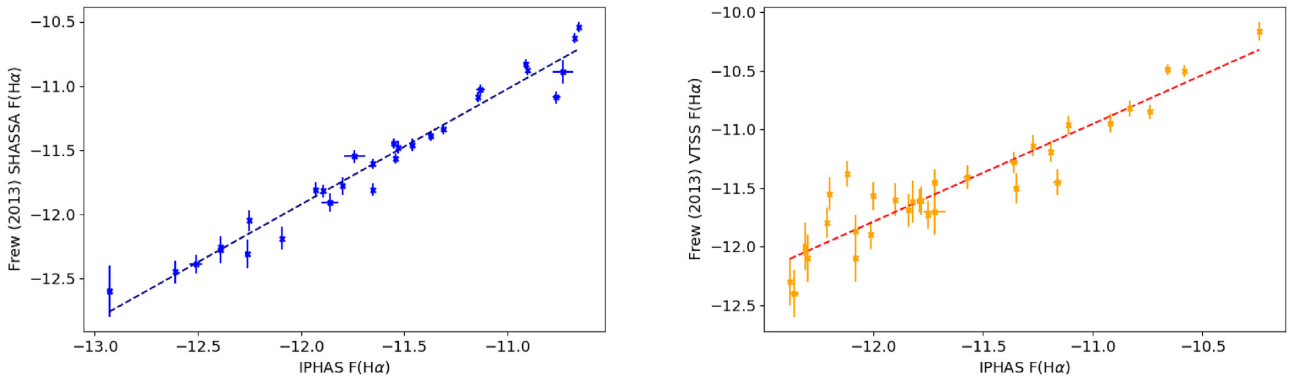

Figure 1. IPHAS Hα log fluxes (in cgs units) compared to the (a) SHASSA (left-hand panel) and (b) VTSS (right-hand panel) Hα log fluxes of Frew, Bojičić & Parker (2013), all after correction for [N II] contributions. The lines of best fit are shown as dashed lines, with slopes of 0.90 ± 0.03 and 0.84 ± 0.06 for the SHASSA and VTSS comparisons, respectively.

The Hα filter magnitudes were converted to in-filter fluxes using a zero-magnitude flux calibration for the Hα filter of 1.57×10^{-7} ergs cm^{-2} s^{-1}. This was obtained by multiplying the mean monochromatic flux for Vega in the Hα filter of 1.81×10^{-9} ergs cm^{-2} s^{-1} Å^{-1} (Barentsen et al. 2014) by an equivalent width of 84.04 Å for the Hα filter that was obtained by integrating across the transmission profile of the filter as a function of wavelength. At the time of the IPHAS DR2 data release, Vega was adopted to have a magnitude of +0.035 at all optical wavelengths. Between DR2 and the most recent release (Greimel at al., in preparation), the calibration changes show a 1σ scatter of ±0.03 magnitudes.

In Appendix A (see Suppl. material), our Hα filter aperture photometry results are presented in column 5 of Table A1, for the IPHAS-discovered PNe, while column 5 of Table A2 presents our photometry for previously catalogued PNe observed by the IPHAS survey. A number of very bright PNe had saturated pixels in their Hα images and were therefore omitted from our sample (e.g. NGC 7027, BD+30°3639, Vy 2-2).

2.4 Correction of the Hα filter fluxes for [N II] contributions

The [N II] λ6548.03 Å and λ6583.41 Å doublet is situated on either side of the Hα λ6562.82 Å line. The INT-WFC Hα filter has an effective wavelength of 6568 Å and a transmission FWHM of 95 Å and its transmission at the wavelengths of the [N II] lines is the same as at Hα to within a few per cent.

To correct the Hα filter fluxes for [N II] line contributions, spectroscopically measured [N II]/Hα flux ratios for each PN were available from the literature for 39 of the 46 IPHAS-discovered PNe and for all 151 of the previously catalogued PNe. If the published spectroscopic data provided the flux for only one line of the [N II] doublet, we corrected for the contribution from both lines assuming an intrinsic 6583/6548 flux ratio of 3.0 (Storey & Zeippen 2000). Column 9 of Table A1 and column 6 of Table A2 list the ([N II] 6583 + 6548)/Hα ratios adopted from the literature, and their sources, while the next column lists log Hα line fluxes after removing the [N II] line contributions. For nebulae where the differences between individual flux measurements were less than 0.01 dex, we set the final uncertainty on the mean flux to be 0.01 dex.

Most spectroscopic [N II]/Hα ratios are based on long-slit spectra. Since observed ratios can sometimes vary significantly with location in extended nebulae, we consider our adopted corrections to be more reliable for those nebulae having angular diameters of less than 5–6 arcsec.

Although the [N II] lines are the major source of contamination of the in-filter Hα fluxes, the continuum from stars within the PN measurement aperture is another potential contaminant, although this is corrected to first order via the subtraction of the flux in the sky aperture. The underlying nebular continuum is another potential contributor, although for the case of the narrow-band WFC Hα filter its contribution is estimated to be minor. Using the NEBCONT routine in the DIPSO package (Howarth et al. 2004) then, for a nebular electron density of 10^3 cm^{-3} and 10^4 K with $n(\mathrm{He}^+)/n(\mathrm{H}^+) = 0.10$, one finds that for a H$\alpha$ flux towards the faint end of the Hα flux distribution shown in Fig. 1, i.e. 10^{-12} ergs cm^{-2} s^{-1}, the in-filter nebular continuum flux in the 95-Å FWHM IPHAS Hα filter would contribute 1.9×10^{-14} ergs cm^{-2} s^{-1}, or 1.9 per cent of the Hα flux. The in-filter flux that would be contributed by a 17th-magnitude central star would be less than 1 per cent of the same nebular Hα flux.

2.5 Comparison with the Hα fluxes of Frew et al. (2013)

Frew et al. (2013) presented a catalogue of Hα fluxes for 1258 Galactic PNe obtained using data from the Southern Hα Sky Survey Atlas (SHASSA) (Gaustad et al. 2001) and the Virginia Tech Spectral-line Survey (VTSS)(VTech 2014)[5]. The VTSS survey used an f/1.2 camera lens with a 58-mm focal length, together with a 512 × 512 CCD array that projected to 96 arcsec per pixel on the sky. Its integration times were not specified. Its Hα filter had an FWHM of 17.5 Å, transmitting mainly the Hα line. The SHASSA survey used an f/1.6 camera lens with a focal length of 52 mm with maximum exposure times of 1200 s on to a 1024 × 1024 CCD array that projected to 48 arscec per pixel on the sky. Its Hα filter had an FWHM of 32 Å and transmissions of 39 per cent, 26 per cent, and 78 per cent at the rest wavelengths of the [N II] 6548, 6583 Å, and Hα lines, respectively (Gaustad et al. 2001). The transmissions of these lines were equal for the 95-Å FWHM Hα filter used by IPHAS. Therefore for the same PN with the same [N II]/Hα ratio, the [N II] contribution to the SHASSA Hα filter flux measured by Frew et al.

[5]http://www.phys.vt.edu/~halpha/

(2013) should be less than that made to the IPHAS WFC H α-filter flux measured here.

Fig. 1(a) plots our measured IPHAS H α fluxes against the SHASSA H α fluxes measured by Frew et al. (2013) for 29 nebulae in common, both after [N II] corrections have been applied. The SHASSA fluxes are on average fainter than the IPHAS fluxes by 0.08 ± 0.12 dex, consistent with no net difference within the uncertainty limits. The slope of the line of best fit is 0.90 ± 0.03.

A similar comparison of the [N II]-corrected IPHAS H α fluxes with the Frew et al. (2013) VTSS H α fluxes for 32 nebulae in common showed the VTSS H α fluxes to be 0.17 ± 0.19 dex brighter than the IPHAS H α fluxes, again consistent with no net difference within the uncertainty limits, with the larger dispersion attributable to the larger uncertainties associated with the VTSS fluxes, see Fig. 1(b).

3 NEBULAR EXTINCTIONS

3.1 Determining dust extinctions to the nebulae

Since the radio free–free fluxes of PNe undergo virtually no extinction by interstellar dust, we can estimate absolute extinctions to PNe at optical wavelengths by comparing their measured hydrogen Balmer line fluxes with Balmer line fluxes predicted from their measured radio free–free fluxes using recombination theory. We have therefore used our measured H α fluxes, as well as H β fluxes from the literature, together with literature radio free–free fluxes, to determine dust extinctions at the wavelengths of the two Balmer lines. The logarithmic extinctions at H β ($C_{H\beta}$) were calculated using the formulation given by Milne & Aller (1975):

$$C_{H\beta} = \log_{10} \frac{3.28 \times 10^{-9} \times S(5\,\mathrm{GHz}) \times t^{-0.4}}{ln(9900 \times t^{1.5}) \times [1 + (1 - x'')y + 3.7x''y]} - \log_{10} F(H\beta), \quad (1)$$

where $S(5\,\mathrm{GHz})$ is the radio flux density at 5 GHz, in Jy, t is the nebular electron temperature in units of 10^4 K, y is the abundance ratio of He to H nuclei, by number, and x'' is the abundance ratio of doubly ionized He to all He atoms. For nebulae where values of t, x'', and y were not available in the literature, they were assumed to have values of 1, 0, and 0.11, respectively. F(H β) is the observed integrated H β flux, listed in Table B1 from the sources given in Appendix B (see Suppl. material).

Logarithmic extinctions at H α ($C_{H\alpha}$) were also calculated using this formulation, after multiplying the first term in equation (1) by 2.85 to allow for a theoretical H α/H β flux ratio of 2.85 for nebulae at an electron temperature of 10^4 K (Storey & Hummer 1995) and replacing the second term by log(H α), the [N II]-corrected IPHAS H α flux.

As well as using 5 GHz radio flux densities taken from the literature, we also made use of flux densities measured at frequencies of 1.4 and 30 GHz (listed in Table B1 in Appendix B, see Suppl. material). For the $C_{H\alpha}$ and $C_{H\beta}$ extinction calculations, we scaled the 1.4 and 30 GHz fluxes to 5 GHz by assuming a $\nu^{-0.1}$ optically thin free–free spectrum.

We also calculated E(H α–H β) reddenings based on the ratio of the [N II]-corrected IPHAS H α flux to the published H β filter flux, using equation (2) below to obtain the colour excess between the H α and H β wave bands:

$$E\,(H\alpha - H\beta) = 2.5 \log_{10}\left(\frac{F(H\alpha)/F(H\beta)}{2.85}\right). \quad (2)$$

Using this colour excess, we were then able to obtain the absolute visual extinction $A_V[E(H\alpha–H\beta)]$ using equation (3) below, which adopts the Galactic Reddening Law of Howarth (1983), with $R_V = A_V/E(B - V) = 3.10$.

$$A_V\,[E\,(H\alpha - H\beta)] = 2.669 \times E(H\alpha - H\beta), \quad (3)$$

where $A_V[E(H\alpha–H\beta)]$ is given in magnitudes. We also adopted the Howarth (1983) reddening law for $R_V = 3.1$ to calculate visual extinctions from $C_{H\alpha}$ ($A_V(C_{H\alpha})$) and $C_{H\beta}$ ($A_V(C_{H\beta})$), using equations (4) and (5):

$$A_V\,(C_{H\alpha}) = 3.140 \times C_{H\alpha} \quad (4)$$

$$A_V\,\left(C_{H\beta}\right) = 2.135 \times C_{H\beta}. \quad (5)$$

Table C1 in Appendix C (see Suppl. material) presents our derived $E(H\alpha–H\beta)$ values for 37 PNe, together with the corresponding values of A_V and $C_{H\beta}$. Table D1 in Appendix D (see Suppl. material) presents the A_V values derived for 143 PNe from the various combinations of the three radio frequency fluxes and the H α and H β fluxes. In order to calculate the uncertainties on all A_V values, standard error propagation was used. In some cases the literature fluxes did not have any listed uncertainties and in such cases A_V values obtained using those fluxes were discarded. For each PN, using the $A_V(C_{H\alpha})$ and $_V(C_{H\beta})$ values corresponding to each of the radio frequencies, 1.4, 5, and 30 GHz, we obtained a weighted mean radio extinction value, A_V(Radio), as listed in the penultimate column of Table D1 (see Suppl. material).

The derived extinctions showing the best interagreement (the maximum allowed variation between the A_V values selected was ± 0.9 magnitudes) are shown in bold script in Table D1 (see Suppl. material) and these were used for obtaining the final weighted averaged A_V(Radio) values. In cases when there were discrepancies between the different radio-based A_V values that were significantly larger than the formal flux uncertainties, the A_V value corresponding to the highest radio frequency was adopted, on the grounds that the higher frequency free–free radio emission was more likely to be optically thin.

For 143 PNe, a weighted mean of A_V(Radio) and $A_V[E(H\alpha–H\beta)]$ was used to generate a final adopted A_V and its uncertainty, which are listed in columns 3 of Table 1.

3.2 Maximum expected extinctions along PN lines of sight

To provide an upper limit to the extinction along the line of sight to each PN, we utilized the NASA/IPAC Infrared Archive (IRSA) *Galactic Dust Reddening and Extinction*[6] website. The site uses the data of Schlegel, Finkbeiner & Davis (1998) who created Galactic dust temperature and dust column maps by combining results from the IRAS 100 μm and *COBE*/DIRBE surveys. Using these maps and a relation between 100 μm surface brightness and visual extinction they were able to infer total extinctions along any given line of sight out of the Galaxy. Schlafly & Finkbeiner (2011) recalibrated the Schlegel et al. (1998) relations (A_V(Schlafly) $= 0.86A_V$(Schlegel)) and so we use the Schlafly & Finkbeiner (2011) values to predict the maximum value of A_V expected along a line of sight. These values are presented in Fig. 2 and in Appendix E (see Suppl. material).

[6] http://irsa.ipac.caltech.edu/applications/DUST/

Table 1. Adopted extinctions and distances derived from Sale et al. (2014) H-MEAD and Green et al. (2019).

PN G	Name	A_V (mag)	H-MEAD (kpc)	Green + 2019 (kpc)
030.8+03.4	Abell 47	8.27 ± 0.33	>10.5	>5.2
031.0+04.1	K 3-6	7.18 ± 0.17	$5.30^{+0.50}_{-0.26}$	>4.5
031.3−00.5	HaTr 10	3.26 ± 0.19	$0.94^{+0.19}_{-0.11}$	$2.33^{+0.74}_{-0.50}$
031.7+01.7	PC 20	5.45 ± 0.10	$4.57^{+0.33}_{-0.33}$	$12.6^{+2.31}_{-4.47}$
032.0−03.0	K 3-18	3.93 ± 0.18	$6.00^{+0.40}_{-0.49}$	>3.42
032.5−03.2	K 3-20	2.13 ± 0.19	$2.45^{+0.77}_{-0.56}$	$3.63^{+0.50}_{-0.59}$
032.9−02.8	K 3-19	3.40 ± 0.10	$6.35^{+0.29}_{-0.36}$	>6.63
033.8−02.6	NGC 6741	1.89 ± 0.03	$2.44^{+0.07}_{-0.06}$	$3.58^{+0.03}_{-0.03}$
035.7−05.0	K 3-26	2.12 ± 0.16	$7.11^{+6.27}_{-0.74}$	>5.2
035.9−01.1	Sh 2-71	1.44 ± 0.13	$0.12^{+0.01}_{-0.01}$	$0.49^{+0.02}_{-0.02}$
036.9−02.6	HaTr 13	2.82 ± 0.25	$2.58^{+0.99}_{-0.65}$	$3.90^{+5.60}_{-0.77}$
036.9−01.1	HaTr 11	5.00 ± 0.11	$8.35^{+0.44}_{-0.33}$	>8.3
039.5−02.7	M 2-47	3.08 ± 0.10	$2.05^{+0.20}_{-0.22}$	>3.6
039.8+02.1	K 3-17	7.93 ± 0.09	$5.42^{+0.30}_{-0.27}$	>6.3
040.3−00.4	Abell 53	4.12 ± 0.11	$0.87^{+0.08}_{-0.05}$	$0.86^{+0.01}_{-0.01}$
040.4−03.1	K 3-30	2.62 ± 0.11	$1.99^{+0.23}_{-0.49}$	$3.99^{+0.74}_{-0.08}$
041.8+04.4	K 3-15	2.41 ± 0.08	>9.00	>4.83
043.0−03.0	M 4-14	2.72 ± 0.06	$4.44^{+0.44}_{-0.43}$	>6.2
043.1+03.8	M 1-65	1.74 ± 0.05	$2.25^{+0.11}_{-0.19}$	$3.22^{+0.19}_{-0.25}$
043.3+02.2	PM 1-276	3.26 ± 0.11	$1.99^{+0.20}_{-0.33}$	$3.03^{+0.29}_{-0.07}$
045.9−01.9	K 3-33	5.30 ± 0.05	$3.21^{+0.09}_{-0.18}$	>16.9
046.3−03.1	PB 9	3.39 ± 0.06	$6.83^{+0.18}_{-0.12}$	>4.3
046.4−04.1	NGC 6803	1.24 ± 0.03	$4.25^{+0.14}_{-0.25}$	$3.65^{+0.45}_{-0.23}$
046.8+02.9	CTSS 4	3.03 ± 0.19	>9.0	>4.3
047.1+04.1	K 3-21	2.77 ± 0.19	$7.32^{+6.68}_{-0.65}$	>4.3
048.0−02.3	PB 10	3.59 ± 0.11	$6.73^{+0.29}_{-0.23}$	>8.8
048.1+01.1	K 3-29	6.89 ± 0.05	>10.0	>9.3
048.5+04.2	K 4-16	2.92 ± 0.06	>7.0	>4.5
048.7+02.3	K 3-24	6.07 ± 0.19	>8.0	>2.5
048.7+01.9	Hen 2-429	3.50 ± 0.10	$6.04^{+0.47}_{-0.63}$	$4.67^{+1.76}_{-0.59}$
049.4+02.4	Hen 2-428	2.86 ± 0.09	$2.90^{+0.36}_{-0.30}$	$3.84^{+0.05}_{-0.09}$
050.4−01.6	K 4-28	5.15 ± 0.06	$5.74^{+0.21}_{-0.11}$	$6.75^{+0.04}_{-0.06}$
051.0−04.5	PC 22	2.10 ± 0.15	>7.0	>5.6
051.0+03.0	Hen 2-430	3.56 ± 0.17	$2.71^{+0.59}_{-0.44}$	$3.14^{+2.13}_{-0.06}$
051.3+01.8	PM 1-295	3.56 ± 0.11	$0.97^{+0.15}_{-0.02}$	$1.40^{+0.08}_{-0.16}$
051.9−03.8	M 1-73	1.57 ± 0.10	$3.46^{+0.66}_{-0.64}$	$4.45^{+0.66}_{-0.72}$
052.2−04.0	M 1-74	1.58 ± 0.12	$6.87^{+0.63}_{-0.87}$	$7.21^{+1.81}$
052.5−02.9	Me 1-1	1.15 ± 0.09	$2.42^{+0.18}_{-0.40}$	$2.73^{+0.52}_{-0.46}$
052.9−02.7	K 3-41	1.44 ± 0.30	$2.74^{+0.46}_{-0.76}$	$2.74^{+0.49}_{-1.07}$
052.9+02.7	K 3-31	4.61 ± 0.08	$4.46^{+0.21}_{-0.23}$	>2.5
053.2−01.5	K 3-38	4.56 ± 0.08	$5.88^{+0.17}_{-0.07}$	$9.74^{+0.04}_{-0.04}$
053.8−03.0	Abell 63	0.67 ± 0.20	$0.92^{+0.25}_{-0.41}$	$0.76^{+0.47}_{-0.19}$
054.2−03.4	Necklace	2.41 ± 0.19	>8.0	>4.3
054.4−02.5	M 1-72	2.03 ± 0.32	$6.82^{+3.12}_{-1.74}$	>5.5
055.1−01.8	K 3-43	3.48 ± 0.27	$6.65^{+0.65}_{-0.80}$	>4.1
055.2+02.8	Hen 2-432	3.40 ± 0.08	$2.50^{+0.31}_{-0.35}$	>3.1
055.3+02.7	Hen 1-1	3.85 ± 0.07	$4.15^{+0.20}_{-0.38}$	>7.8
055.5−00.5	M 1-71	4.39 ± 0.13	$7.01^{+0.19}_{-0.23}$	$9.55^{+0.02}_{-0.02}$
055.6+02.1	Hen 1-2	2.78 ± 0.07	$0.28^{+1.11}_{-0.02}$	$2.50^{+0.23}_{-0.20}$
056.0+02.0	K 3-35	6.63 ± 0.17	$9.96^{+4.38}_{-1.21}$	>10.9
056.4−00.9	K 3-42	5.24 ± 0.07	$8.38^{+0.20}_{-0.19}$	$10.5^{+0.03}_{-0.03}$

Table 1 – *continued*

PN G	Name	A_V (mag)	H-MEAD (kpc)	Green + 2019 (kpc)
057.9−01.5	Hen 2-447	4.42 ± 0.05	$6.77^{+0.05}_{-0.21}$	>8.0
058.9+01.3	K 3-40	3.00 ± 0.08	$5.43^{+0.15}_{-0.17}$	$6.64^{+0.16}_{-0.64}$
059.4+02.3	K 3-37	4.33 ± 0.07	$7.20^{+0.25}_{-0.21}$	>7.5
059.0+04.6	K 3-34	2.57 ± 0.29	>7.0	>4.7
059.9+02.0	K 3-39	4.41 ± 0.07	$7.76^{+0.26}_{-0.23}$	>7.0
060.4+01.5	PM 1-310	4.96 ± 0.27	>8.0	>5.8
060.5−00.3	K 3-45	4.91 ± 0.19	$5.33^{+0.56}_{-0.65}$	$10.1^{+1.22}_{-0.45}$
060.5+01.8	Hen 2-440	3.93 ± 0.05	$8.47^{+0.28}_{-0.25}$	$11.1^{+0.04}_{-0.04}$
060.8−03.6	NGC 6853	0.10 ± 0.14	$0.11^{+0.07}_{-0.04}$	$0.96^{+0.02}_{-0.08}$
062.4−00.2	M 2-48	3.45 ± 0.15	$2.75^{+0.29}_{-0.55}$	$3.30^{+0.06}_{-0.03}$
063.8−03.3	K 3-54	4.82 ± 0.22	$5.30^{+0.49}_{-0.21}$	>4.3
064.9−02.1	K 3-53	2.91 ± 1.02	$3.88^{+2.84}_{-2.57}$	$3.27^{+11.7}_{-2.21}$
065.1−03.5	We 1-9	3.16 ± 1.02	$1.34^{+3.48}_{-0.62}$	$1.60^{+13.3}_{-0.58}$
065.9+00.5	NGC 6842	2.51 ± 0.11	$4.34^{+0.16}_{-0.10}$	$4.85^{+0.04}_{-0.04}$
066.9+02.2	K 4-37	4.25 ± 0.19	>7.0	>8.8
067.9−00.2	K 3-52	8.46 ± 0.18	>8.0	>7.8
068.3−02.7	Hen 2-459	4.61 ± 0.05	$5.44^{+0.09}_{-0.04}$	>5.0
068.6+01.1	Hen 1-4	2.36 ± 0.11	$3.40^{+0.66}_{-0.31}$	$3.10^{+0.25}_{-0.07}$
068.7+01.9	K 4-41	3.72 ± 0.32	>8.5	$11.5^{+0.19}_{-0.20}$
068.7+03.0	PC 23	3.66 ± 0.21	>7.0	>6.7
068.8−00.0	M 1-75	4.20 ± 0.19	$6.20^{+0.25}_{-0.67}$	$7.75^{+1.16}_{-4.53}$
069.2+03.8	K 3-46	2.15 ± 0.26	$4.73^{+1.49}_{-1.80}$	$5.92^{+9.03}_{-2.50}$
069.2+02.8	K 3-49	3.37 ± 0.07	>8.0	>3.5
069.4−02.6	NGC 6894	1.40 ± 0.14	$1.01^{+0.01}_{-0.01}$	$1.43^{+0.14}_{-0.07}$
069.6−03.9	K 3-58	4.11 ± 0.19	>7.0	>5.5
069.7+00.0	K 3-55	7.05 ± 0.16	>8.0	>8.5
071.6−02.3	M 3-35	4.61 ± 0.08	$4.57^{+0.30}_{-0.27}$	>5.5
072.1+00.1	K 3-57	5.35 ± 0.33	$9.94^{+3.88}_{-1.75}$	>5.1
073.0−02.4	K 3-76	4.27 ± 0.29	$4.30^{+0.45}_{-0.57}$	>5.4
074.5+02.1	NGC 6881	3.60 ± 0.03	$5.15^{+0.16}_{-0.05}$	$5.87^{+0.05}_{-0.05}$
075.6+04.3	ARO 342	2.26 ± 0.19	>7.0	>4.7
076.3+01.1	Abell 69	4.20 ± 0.17	$5.50^{+0.16}_{-0.19}$	$6.25^{+0.12}_{-0.12}$
076.4+01.8	KjPn 3	3.42 ± 0.19	$5.02^{+0.49}_{-0.28}$	$4.86^{+0.46}_{-0.63}$
077.5+03.7	KjPn 1	1.50 ± 0.21	$2.36^{+0.74}_{-0.33}$	$2.28^{+0.35}_{-0.68}$
077.7+03.1	KjPn 2	5.51 ± 0.19	$6.89^{+2.24}_{-0.87}$	>4.6
078.3−02.7	K 4-53	4.88 ± 0.10	$9.31^{+4.69}_{-2.02}$	>3.9
078.9+00.7	Sd 1	5.06 ± 0.19	$2.84^{+0.23}_{-0.17}$	$1.07^{+0.01}_{-0.01}$
084.2+01.0	K 4-55	2.94 ± 0.18	$0.63^{+0.10}_{-0.01}$	$1.17^{+0.33}_{-0.38}$
084.9+04.4	Abell 71	2.44 ± 0.11	$2.26^{+0.08}_{-0.04}$	$2.44^{+0.01}_{-0.01}$
088.7+04.6	K 3-78	4.47 ± 0.05	$7.70^{+6.30}_{-1.41}$	>3.2
088.7−01.6	NGC 7048	0.82 ± 0.04	$2.03^{+0.05}_{-0.06}$	$1.99^{+0.34}_{-0.75}$
089.0+00.3	NGC 7026	1.77 ± 0.05	$2.15^{+0.11}_{-0.11}$	$2.68^{+0.01}_{-0.01}$
089.8−00.6	Sh 1-89	3.52 ± 0.20	$3.39^{+0.40}_{-0.18}$	$5.99^{+0.06}_{-0.40}$
091.6−04.8	K 3-84	1.25 ± 0.24	$6.83^{+7.17}_{-2.01}$	>4.3
091.6+01.8	We 1-11	4.43 ± 0.06	$2.16^{+0.11}_{-0.04}$	$2.07^{+0.20}_{-0.13}$
093.3−00.9	K 3-82	3.72 ± 0.14	$4.75^{+0.15}_{-0.13}$	>7.8
093.3−02.4	M 1-79	0.84 ± 0.04	$2.31^{+0.17}_{-0.20}$	$1.33^{+0.14}_{-0.25}$
094.5−00.8	K 3-83	4.75 ± 0.04	$14.0^{+0.47}_{-2.5}$	>9.1
095.1−02.0	M 2-49	3.67 ± 0.06	$8.05^{+0.78}_{-0.51}$	>5.1
095.2+00.7	K 3-62	5.35 ± 0.04	$5.37^{+0.04}_{-0.04}$	>8.2
096.3+02.3	K 3-61	3.78 ± 0.05	$3.25^{+0.20}_{-0.14}$	$8.59^{+2.37}_{-0.12}$

Table 1 – *continued*

PN G	Name	A_V (mag)	H-MEAD (kpc)	Green + 2019 (kpc)
097.6−02.4	M 2-50	2.01 ± 0.05	>6.0	>8.0
098.1+02.4	K 3-63	2.54 ± 0.08	$2.84^{+0.39}_{-0.41}$	$3.70^{+0.29}_{-0.19}$
098.2+04.9	K 3-60	4.55 ± 0.05	>5.0	>2.8
102.8−05.0	Abell 80	0.12 ± 0.06	$1.54^{+0.43}_{-0.45}$	$0.33^{+0.05}_{-0.03}$
103.2+00.6	M 2-51	1.79 ± 0.08	$1.60^{+0.10}_{-0.07}$	$2.33^{+0.05}_{-0.04}$
103.7+00.4	M 2-52	2.91 ± 0.05	$4.19^{+0.04}_{-0.06}$	$3.85^{+0.02}_{-0.02}$
104.1+01.0	Bl 2-1	5.31 ± 0.04	$5.26^{+0.09}_{-0.09}$	>4.8
104.4−01.6	M 2-53	2.41 ± 0.05	$2.09^{+0.07}_{-0.05}$	>4.8
107.4−02.6	K 3-87	4.45 ± 0.12	>6.0	>3.7
107.4−00.6	K 4-57	3.85 ± 0.19	>6.0	>10.7
107.7−02.2	M 1-80	1.64 ± 0.05	$4.33^{+0.25}_{-0.26}$	$5.09^{+0.18}_{-0.51}$
107.8+02.3	NGC 7354	3.70 ± 0.03	$2.12^{+0.06}_{-0.03}$	$2.56^{+0.49}_{-0.04}$
112.5−00.1	KjPn 8	1.80 ± 0.11	$2.36^{+0.03}_{-0.26}$	$2.88^{+0.24}_{-0.11}$
112.5+03.7	K 3-88	4.65 ± 0.06	>5.0	>3.3
119.3+00.3	BV 5-1	2.52 ± 0.05	$4.56^{+0.14}_{-0.07}$	>5.5
121.6+00.0	BV 5-2	2.43 ± 0.06	$1.89^{+0.15}_{-0.13}$	$3.40^{+0.03}_{-0.04}$
121.6+03.5	We 1-1	4.05 ± 0.06	$3.28^{+0.06}_{-0.18}$	>2.1
122.1−04.9	Abell 2	1.75 ± 0.05	>5.0	>2.9
126.3+02.9	K 3-90	2.76 ± 0.05	$3.92^{+0.08}_{-0.07}$	>3.9
126.6+01.3	IPHAS PN-1	1.47 ± 1.05	$0.10^{+2.14}_{-0.03}$	$0.76^{+2.89}_{-0.45}$
129.5+04.5	K 3-91	3.51 ± 0.05	>4.5	>2.3
130.2+01.3	IC 1747	2.02 ± 0.04	$4.20^{+0.12}_{-0.21}$	$4.64^{+0.08}_{-0.07}$
130.4+03.1	K 3-92	1.96 ± 0.19	$4.42^{+0.39}_{-0.90}$	$4.81^{+10.1}_{-1.53}$
131.5+02.6	Abell 3	0.44 ± 0.06	$0.43^{+0.02}_{-0.18}$	$0.26^{+0.05}_{-0.02}$
132.4+04.7	K 3-93	3.74 ± 0.06	>4.5	>2.3
136.1+04.9	Abell 6	2.14 ± 0.19	$0.46^{+0.22}_{-0.03}$	$1.00^{+0.05}_{-0.05}$
138.8+02.8	IC 289	2.33 ± 0.02	$0.96^{+0.01}_{-0.01}$	$3.82^{+0.03}_{-0.03}$
142.1+03.4	K 3-94	2.84 ± 0.15	>5.0	>3.5
147.4−02.3	M 1-4	3.23 ± 0.06	$2.75^{+0.07}_{-0.09}$	>4.0
147.8+04.1	M 2-2	2.95 ± 0.15	$4.55^{+9.45}_{-0.45}$	>3.0
151.4+00.5	K 3-64	3.28 ± 0.25	$9.98^{+4.02}_{-3.54}$	>10.2
173.5+03.2	Pu 2	3.95 ± 0.17	$3.22^{+0.25}_{-0.26}$	>1.5
178.3−02.5	K 3-68	2.73 ± 0.19	$8.88^{+5.12}_{-4.04}$	>5.3
181.5+00.9	Pu 1	2.55 ± 0.06	$10.1^{+3.94}_{-2.1}$	>4.7
184.0−02.1	M 1-5	2.84 ± 0.02	>4.5	>5.1
184.6+00.6	K 3-70	4.13 ± 0.12	>5.0	>5.0
184.8+04.4	K 3-71	3.52 ± 0.27	>4.0	>2.6
194.2+02.5	J 900	1.64 ± 0.03	>4.5	>10.2
201.7+02.5	K 4-48	3.05 ± 0.10	>4.0	>4.4
210.3+01.9	M 1-8	2.48 ± 0.21	>5.0	>3.5
212.0+04.3	M 1-9	1.17 ± 0.07	$2.90^{+0.58}_{-0.76}$	>4.1

4 EXTINCTION DISTANCES TO GALACTIC PLANETARY NEBULAE

The technique that we adopt for determining distances to the northern Galactic PNe in our IPHAS sample is the 3D extinction mapping method, which uses an extinction versus distance relationship derived from field stars nearby on the sky to each PN in order to estimate its distance (see Lutz 1973; Gathier et al. 1986; Giammanco et al. 2011). In this paper, we make use of three recent Galactic extinction versus distance mapping tools that are based on independent large stellar photometric data bases. In Section 4.1 we derive extinction distances using the IPHAS-based H-MEAD 3D extinction mapping algorithm (Sale et al. 2014). In Section 4.2 we present distances obtained using the Pan-STARRS 1/2MASS-based BAYESTAR2019 3D extinction mapping tool (Green et al. 2019), while in Section 4.3 we make a limited comparison with distances obtained using the *Gaia*/2MASS-based STILISM 3D reddening mapping tool (Lallement et al. 2019). In Section 4.4 we compare distances obtained using each of the above tools with reliable *Gaia* DR2 distances that are available for 17 of the PNe in our sample.

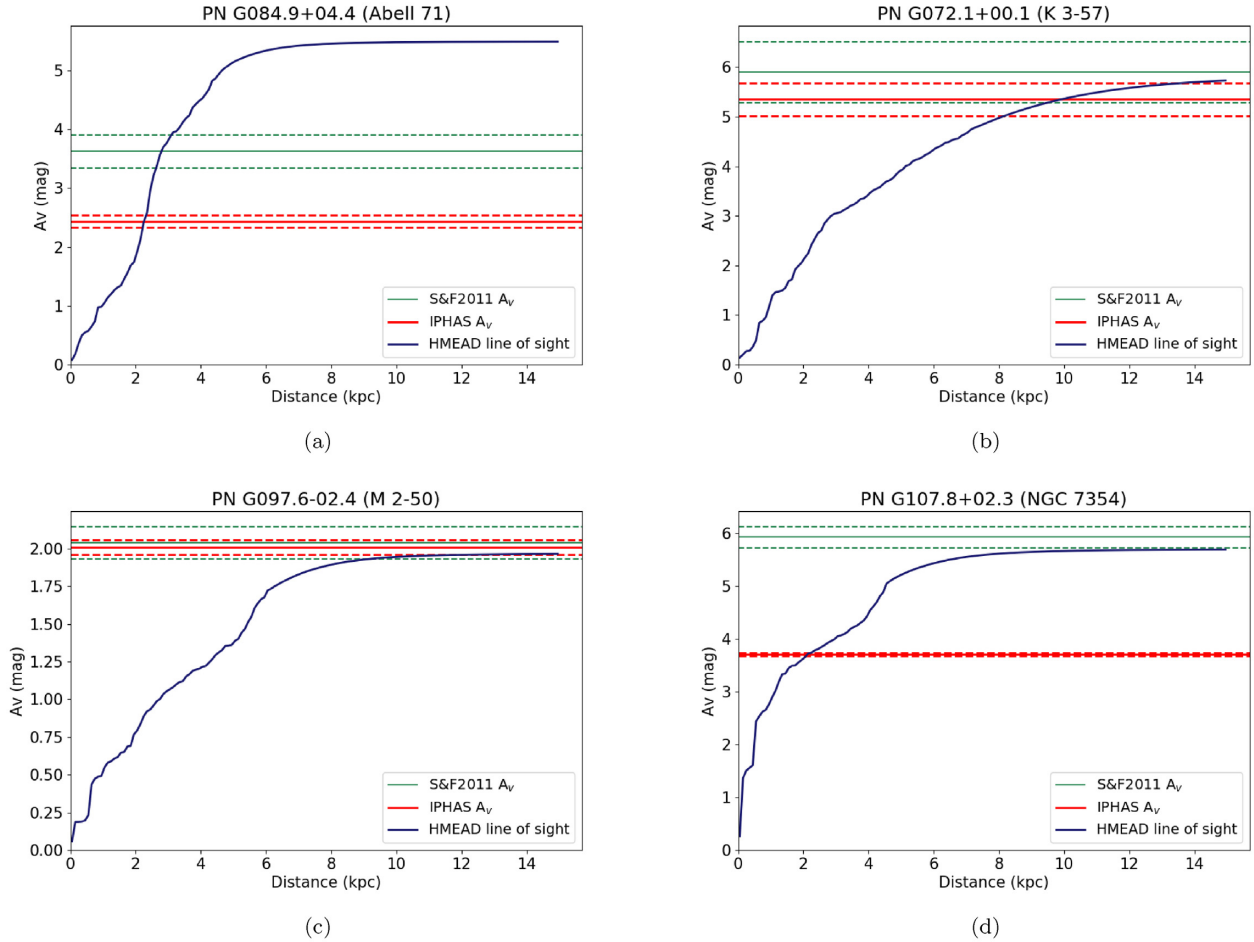

Figure 2. H-MEAD distance-extinction relationships for the sightlines to (a) Abell 71 ($l = 85.00$, $b = +4.49$), (b) K 3-57 ($l = 72.20$, $b = +0.10$), (c) M 2-50 ($l = 97.68$, $b = -2.45$), and (d) NGC 7354 ($l = 107.84$, $b = +2.32$). The solid blue curve in each plot represents the H-MEAD extinction versus distance relation for the sightline to the nebula. The solid and dashed red horizontal lines correspond to the value of A_V derived for the nebula, and its corresponding uncertainties, while the solid and dashed green horizontal lines correspond to the Schlafly & Finkbeiner (2011) A_V limit and its uncertainties.

4.1 Distances using the H-MEAD 3D extinction mapping algorithm

This method rests on photometric data from the IPHAS survey in building distance–extinction relationships for A–K stars across the northern Plane. The source for the extinction–distance relations along the relevant lines of sight is the H-MEAD algorithm (Hierarchical Mapper of Extinction Against Distance) described by Sale (2012) and implemented by Sale et al. (2014). H-MEAD uses hierarchical Bayesian principles to determine the required properties of all the available A–K stars within any specified square pencil beam (voxel) in order to derive a mean relation between increasing extinction and distance.

To give a little more detail, Sale et al. (2014) used the IPHAS ($r' - i'$) and ($r' - \mathrm{H}\,\alpha$) colour–colour plane to assign (probabilistically) spectral type and luminosity class to every detected star in the voxel of interest. The algorithm rejects any objects that are not plausible A–K stars. This information constrains each accepted star's likely absolute magnitude and monochromatic extinction at 5495 Å (A_0, a quantity that is for most purposes nearly identical to the band mean, A_V). These data, along with the IPHAS apparent magnitudes, are then used to calculate distances to all the retained stars, which are then dynamically binned according to their distances: each bin contains a minimum of eight stars and is at least 100 pc in depth. H-MEAD takes into account sources of inaccuracy, scatter and bias such as photometric error, unresolved ISM substructure within the voxel, binarity, and photometric magnitude limits (see also Sale et al. 2009; Giammanco et al. 2011).

The photometric depth of the IPHAS survey enabled the northern Galactic Plane to be extinction-mapped by Sale et al. (2014) with voxel sizes ranging from 5×5 arcmin^2 at the highest stellar densities up to, very occasionally, 60×60 arcmin^2 in the darkest regions. This variation is in response to the requirement of at least 200 stars to work with, within the voxel. The most frequent angular resolution is 10×10 arcmin^2. The useful distance range is usually from 1 up to 10 kpc, set by the bright and faint limits of the survey photometry, respectively.

The H-MEAD distance–extinction relationship curves from Sale et al. (2014) that we selected as best matching each of the PN sightlines were obtained from the website http://www.iphas.org/data/extinction.

Once the appropriate distance–extinction relation for the voxel enclosing the coordinates of a PN had been identified and downloaded, it was simply a matter of plotting it and reading off the distance corresponding to the final averaged A_V of the PN. The uncertainty on this distance was found by obtaining the distances corresponding to the upper and lower limits for A_V. We were able to do this for 143 PNe

– examples are shown in Fig. 2. The distance–extinction relationships for all the sightlines analysed are presented in Appendix E (see Suppl. material). The cut-off distance in all of them is 14 kpc.

The distance–extinction curves typically begin with a sharp increase in A_V and end as a plateau with very little subsequent increase in A_V with distance. A sharp jump in extinction over a small distance range will be due to the presence of a dense interstellar cloud extinguishing the starlight. There are two reasons for the terminal plateaus commonly seen. The first is that the dust layer is physically thin (100 pc or so above/below the Galactic equatorial plane) and is exited more quickly for sightlines at higher Galactic latitude. Lines of sight at high Galactic latitudes tend to run out of after a few kpc. This can be seen for the PN Abell 71 ($b = +4.49^\circ$) whose distance–extinction relationship is shown in Fig. 2. Its curve reaches a plateau at a heliocentric distance of ~ 4 kpc. The second factor that can be at work, particularly at low Galactic latitudes within the Solar Circle, is high extinction limiting the detected stars to within a short distance – forcing H-MEAD to rely on the prior in extending the curve further out. In such cases the prior can impose the plateau (see Sale et al. 2014). The distance–extinction relationship for K 3-57 ($l = 72.20^\circ$, $b = 00.10^\circ$), shown in Fig. 2, is a good example of this.

It is unavoidable that this method of distance estimation does not always deliver a useful result. For some PNe the derived value of A_V is above the maximum A_V of the plateau region of the relevant extinction–distance curve but below the A_V(Schlafly) value for the sightline. Where this happens, it is likely that more heavily reddened field stars along the line of sight were fainter than the IPHAS survey limits. In cases of PNe with A_V falling in the plateau region of the extinction–distance relationship, the uncertainties on their estimated distances will be much larger, as shown by the relationship for M 2-50 in Fig. 2. Seventeen PNe were found to have A_V values larger than the maximum A_V for their H-MEAD extinction–distance curve as well as lying above the uncertainty limits for the corresponding A_V(Schlafly) values. Five of those 17 PNe are located between $l = 184$ and $l = 202$ deg. In some of these cases this could be due to overestimated extinction values due to errors in the adopted radio fluxes or in the adopted [N II]/H α correction factors. Another possibility is that there might be significant variations of A_V within some of the 10×10 arcmin^2 voxels used to sample the sightlines. We consider it unlikely that significant internal dust extinction within the PNe themselves is the cause of such discrepancies. There are only a few confirmed cases of PNe with large internal dust extinctions (e.g. NGC 7027, NGC 6302) – typical bright PNe such as NGC 7009 have been found to have relatively small internal dust columns (Walsh et al. 2016).

The extinction–distance relationship for NGC 7354 shown in Fig. 2 is an example of a well-behaved curve, where the calculated A_V for the PN lies on the sharply increasing portion of the curve, and where the A_V(Schlafly) value lies above the A_V limit corresponding to the plateau region of the extinction–distance curve.

The measured distances to all 143 PNe are listed in column 4 of Table 1. For PNe which had calculated A_V values greater than the H-MEAD curve's maximum A_V limit, they were assigned a minimum distance corresponding to just after the onset of the final plateau in the H-MEAD extinction curve.

4.2 Distances using the BAYESTAR2019 3D extinction mapping algorithm

Green et al. (2019) have constructed a 3D dust reddening map for the sky north of declination -30°. By making use of Pan-STARRS 1 optical photometry, 2MASS near-infrared photometry, and *Gaia* DR2 parallaxes and applying a hierarchical Bayesian model (BAYESTAR2019), they inferred distances, reddenings, and types for 800 million stars in order to create a 3D dust map extending beyond several kpc, which can be accessed at doi:10.7910/DVN/2EJ9TX. We made use of this map to estimate distances for the PNe in our samples, using reddening values corresponding to the extinctions listed in Table 1. The resulting distance estimates, or lower limits, are listed in the final column of the same table. As was the case with H-MEAD distance estimates, where PNe had calculated A_V values that were greater than the maximum A_V limits of the BAYESTAR2019 curves, they were assigned a minimum distance corresponding to just after the onset of the final plateau in the extinction curves.

4.3 Distances using the STILISM 3D extinction mapping algorithm

We have also used the STILISM 3D reddening mapping algorithm of Lallement et al. (2019) (see https://astro.acri-st.fr/gaia_dev/), to estimate reddening distances to PNe in our sample. Because the algorithm makes use of stars having 5σ or better *Gaia* DR2 parallaxes, for most directions this tool does not reach beyond distances of $\sim$3 kpc and so provides only lower limits to the distances to the majority of the PNe in our sample. However, STILISM distances, or lower limits, are listed in column 8 of Table 2 for 17 of the PNe in our sample that are judged to have reliable *Gaia* DR2 distances.

4.4 Comparison with *Gaia* DR2 distances

For a subset of the PNe in our sample that were judged to have reliable central star distances from *Gaia* DR2 parallaxes, we can compare these reliable astrometric distances with the distances estimated using the different reddening mapping methods.

The following criteria were used to select the PNe in our sample as having reliable central star parallaxes in the *Gaia* DR2 archive (Gaia Collaboration 2018): (i) the number of effective *Gaia* visits, $N_{per} \geq 8$; (ii) a parallax signal-to-noise ratio >3.4; (iii) a normalized unit-weighted error $u/u_0(G, B_P - R_P) < 1.4$, where $u = \sqrt{\chi^2/(N-5)}$ and $u_0(G, B_P - R_P)$ is the magnitude and colour-dependent reference value.[7] 17 of the PNe in our sample satisfied these criteria. Table 2 lists *Gaia* DR2 parallaxes[8] in column 3, followed in column 4 by the distances obtained by inverting the parallaxes and in column 5 by *Gaia* DR2 distances from Bailer-Jones et al. (2018) that are based on a weak distance prior and which are often adopted for stars with lower signal-to-noise *Gaia* DR2 parallaxes. For the sample of 17 PNe listed in Table 2, the *Gaia* DR2 parallaxes are of sufficiently high reliability that the Bailer-Jones et al. (2018) distances agree closely with the inverted parallax distances. One of the PNe listed in Table 2 has a pre-*Gaia* parallax measurement. Benedict et al. (2009) reported a parallax of 2.47 ± 0.16 mas for the central star of NGC 6853, versus the *Gaia* DR2 parallax of 2.658 ± 0.044 mas.

For comparison with the above *Gaia* DR2 PN central star distances, column 6 of Table 2 lists the PN distances obtained using the H-MEAD extinction mapping method of Sale et al. (2014), while column 7 lists the distances obtained using the BAYESTAR2019 extinction mapping method of Green et al. (2019). Column 8 of Table 2 provides Lallement et al. (2019) STILISM distances for 10

[7] See *Gaia* mission document GAIA-C3-TN-LU-LL-124-01 by L. Lindegren at www.rssd.esa.int/doc_fetch.php?id = 3757412

[8] As recommended by Lindegren et al. (2018), the published *Gaia*-DR2 parallaxes have been increased by 0.03 mas to allow for the global zero-point of -0.03 mas.

Table 2. Comparison to *Gaia* DR2 distances.

PN G	Name	*Gaia* DR2 Parallax (mas)	*Gaia* DR2 Parallax distance (kpc)	*Gaia* DR2 Bailer-Jones +2018 (kpc)	H-MEAD (kpc)	Green + 2019 (kpc)	Lallement + 2019 (kpc)	Frew + 2016 (kpc)
035.9−01.1	Sh 2-71	0.588 ± 0.035	$1.62^{+0.10}_{-0.08}$	$1.62^{+0.10}_{-0.09}$	$0.12^{+0.01}_{-0.01}$	$0.49^{+0.02}_{-0.02}$	$0.76^{+0.11}_{-0.05}$	1.32 ± 0.47
043.1+03.8	M 1-65	0.224 ± 0.040	$3.94^{+0.74}_{-0.53}$	$3.90^{+0.74}_{-0.55}$	$2.25^{+0.11}_{-0.19}$	$3.22^{+0.19}_{-0.25}$	$1.68^{+0.06}_{-0.03}$	6.85 ± 2.01
048.5+04.2	K 4-16	0.191 ± 0.053	$4.53^{+1.37}_{-0.86}$	$4.39^{+1.32}_{-0.86}$	>7.0	>4.5	>3.0	11.1 ± 3.5
051.3+01.8	PM 1-295	0.339 ± 0.030	$2.71^{+0.24}_{-0.20}$	$2.72^{+0.24}_{-0.21}$	$1.40^{+0.08}_{-0.16}$	$1.21^{+0.03}_{-0.03}$	>3.5	–
052.5−02.9	Me 1-1	0.226 ± 0.037	$3.91^{+0.67}_{-0.49}$	$3.87^{+0.65}_{-0.49}$	$2.42^{+0.18}_{-0.40}$	$2.73^{+0.52}_{-0.46}$	$2.91^{+0.87}_{-0.57}$	6.17 ± 1.87
053.8−03.0	Abell 63	0.361 ± 0.034	$2.55^{+0.25}_{-0.20}$	$2.57^{+0.26}_{-0.21}$	$0.92^{+0.25}_{-0.41}$	$0.76^{+0.47}_{-0.19}$	$0.63^{+0.47}_{-0.11}$	3.79 ± 1.12
060.8−03.6	NGC 6853	2.658 ± 0.044	$0.37^{+0.01}_{-0.01}$	$0.37^{+0.01}_{-0.01}$	$0.11^{+0.07}_{-0.04}$	$0.96^{+0.02}_{-0.08}$	$0.42^{+0.10}_{-0.23}$	0.31 ± 0.09
065.9+00.5	NGC 6842	0.476 ± 0.046	$1.98^{+0.20}_{-0.16}$	$1.99^{+0.21}_{-0.17}$	$4.34^{+0.16}_{-0.10}$	$4.85^{+0.04}_{-0.04}$	$2.15^{+0.10}_{-0.09}$	2.20 ± 0.64
069.4−02.6	NGC 6894	0.839 ± 0.131	$1.15^{+0.21}_{-0.15}$	$1.18^{+0.24}_{-0.17}$	$1.01^{+0.01}_{-0.01}$	$1.43^{+0.14}_{-0.07}$	$1.17^{+0.04}_{-0.02}$	1.50 ± 0.43
069.7+00.0	K 3-55	0.600 ± 0.071	$1.58^{+0.20}_{-0.15}$	$1.61^{+0.22}_{-0.17}$	>8.0	>8.5	>3.0	3.54 ± 1.32
076.4+01.8	KjPn 3	0.307 ± 0.090	$2.97^{+1.09}_{-0.63}$	$2.89^{+1.02}_{-0.63}$	$5.02^{+0.49}_{-0.28}$	$4.86^{+0.46}_{-0.63}$	$2.61^{+1.20}_{-1.15}$	17.2 ± 4.9
107.8+02.3	NGC 7354	0.454 ± 0.085	$2.07^{+0.45}_{-0.31}$	$2.10^{+0.50}_{-0.35}$	$2.12^{+0.06}_{-0.03}$	$2.56^{+0.49}_{-0.04}$	>3.0	1.26 ± 0.37
130.2+01.3	IC 1747	0.308 ± 0.051	$2.95^{+0.51}_{-0.38}$	$2.95^{+0.54}_{-0.40}$	$4.20^{+0.12}_{-0.21}$	$4.64^{+0.08}_{-0.07}$	>3.5	3.08 ± 1.00
131.5+02.6	Abell 3	0.343 ± 0.084	$2.68^{+0.78}_{-0.49}$	$2.70^{+0.86}_{-0.54}$	$0.43^{+0.02}_{-0.18}$	$0.26^{+0.05}_{-0.02}$	$0.37^{+0.01}_{-0.01}$	2.47 ± 0.73
136.1+04.9	Abell 6	1.004 ± 0.177	$0.97^{+0.20}_{-0.14}$	$1.01^{+0.25}_{-0.17}$	$0.46^{+0.22}_{-0.03}$	$1.00^{+0.05}_{-0.05}$	$1.10^{+0.10}_{-0.07}$	1.30 ± 0.39
138.8+02.8	IC 289	0.628 ± 0.060	$1.52^{+0.15}_{-0.13}$	$1.53^{+0.16}_{-0.13}$	$0.96^{+0.01}_{-0.01}$	$3.82^{+0.03}_{-0.03}$	>3.5	1.88 ± 0.58
147.8+04.1	M 2-2	0.192 ± 0.054	$4.54^{+1.46}_{-0.91}$	$4.26^{+1.23}_{-0.82}$	$4.55^{+9.45}_{-0.45}$	>3.0	>3.0	5.22 ± 1.51

of the 17 PNe that have reliable *Gaia* distances. Finally, column 9 of Table 2 lists PN distances from Frew et al. (2016), a widely used statistical distance estimator that is based on a Hα surface brightness–radius relation for PNe.

Fig. 3 plots the *Gaia* DR2 distances of Bailer-Jones et al. (2018) against the distance estimates obtained from (i) H-MEAD (Sale et al. 2014); (ii) Green et al. (2019); (iii) Lallement et al. (2019); and (iv) Frew et al. (2016). The Pearson correlation coefficient (r) and the corresponding probability value (p) for a null correlation have been calculated for each plot (lower limits to distances were not used). In descending order of their correlation with the *Gaia* DR2 distances are the Frew et al. (2016) distances ($r = 0.61$, $p = 0.012$; 16 PNe), the H-MEAD distances ($r = 0.58$, $p = 0.023$; 15 PNe), the Lallement et al. (2019) distances ($r = 0.57$, $p = 0.085$; for 10 PNe at distances < 3 kpc), with the Green et al. (2019) distances yielding $r = 0.35$ and a p value of 0.22 for 14 PNe.

Giammanco et al. (2011) used the MEAD reddening-distance algorithm of Sale et al. (2009) to estimate reddening distances for 70 PNe located in IPHAS fields, using reddening estimates that were based mainly on spectroscopic Hα/Hβ ratios taken from the literature. Only seven of the seventeen PNe in Table 2 have distance estimates from Giammanco et al. (2011) that are not upper or lower limits, so we have not estimated their correlation coefficient with the *Gaia* DR2 distances.

5 DISCUSSION AND CONCLUSIONS

Using aperture photometry we have measured in-band IPHAS Hα filter fluxes for 46 PNe discovered by IPHAS and for 151 previously catalogued PNe. These in-band fluxes were corrected for [N II] 6548,6583 Å contributions using published spectroscopic [N II]/Hα ratios for 39 of the IPHAS-discovered PNe and for all 151 of the previously catalogued PNe. Radio free–free flux measurements at 1.4, 5, or 30 GHz were available from the literature for 143 of the previously catalogued PNe and these were combined with the [N II]-corrected Hα fluxes and with previously published Hβ filter fluxes to give a weighted mean extinction estimate for each PN from its radio free–free to optical Balmer line flux ratios.

We have used these derived interstellar extinctions with the IPHAS-based H-MEAD interstellar extinction mapping tool of Sale et al. (2014) in order to estimate distances to each PN from the H-MEAD extinction versus distance plot for each sight line. For comparison purposes, we have also estimated extinction distances to the PNe using the Green et al. (2019) extinction mapping tool, which is based on Pan-STARRS 1 and 2MASS photometry and *Gaia* parallaxes. *Gaia* DR2 distances that were judged to be reliable were available for 17 of the PNe in our sample and these distances were compared to the H-MEAD and Green et al. extinction distances for this sub-sample, as well as to a smaller number of extinction distances obtained using the Lallement et al. (2019) extinction mapping tool. We also compared the *Gaia* DR2 distances for this sub-sample with the widely used PN distances from Frew et al. (2016) that are based on a relation between nebular radius and nebular Hα surface brightness. For the sub-sample of 17 PNe, the Frew et al. and the H-MEAD distances were found to show similar degrees of correlation with *Gaia* DR2 distances.

Given that 3D extinction mapping tools are expected to become increasingly sophisticated and to achieve higher angular resolution over time, the weakest link may often be the accuracy of reddening estimates, which need to be significantly improved for many objects. In the case of PNe, reddening values based on observed Balmer line ratios cover too small a wavelength range to be considered ideal. Radio free–free to optical Balmer line ratios cover a much larger wavelength baseline and yield total dust extinctions at the wavelengths of the Balmer lines, but currently many PNe either have no measured radio fluxes or have radio fluxes with relatively low signal-to-noise ratios. More accurate radio flux measurements, over a range of radio wavelengths, are needed. For the northern PNe with IPHAS Hα fluxes that have been discussed here, the ongoing Very Large Array Sky Survey (VLASS; Lacy et al. 2020) will help reach

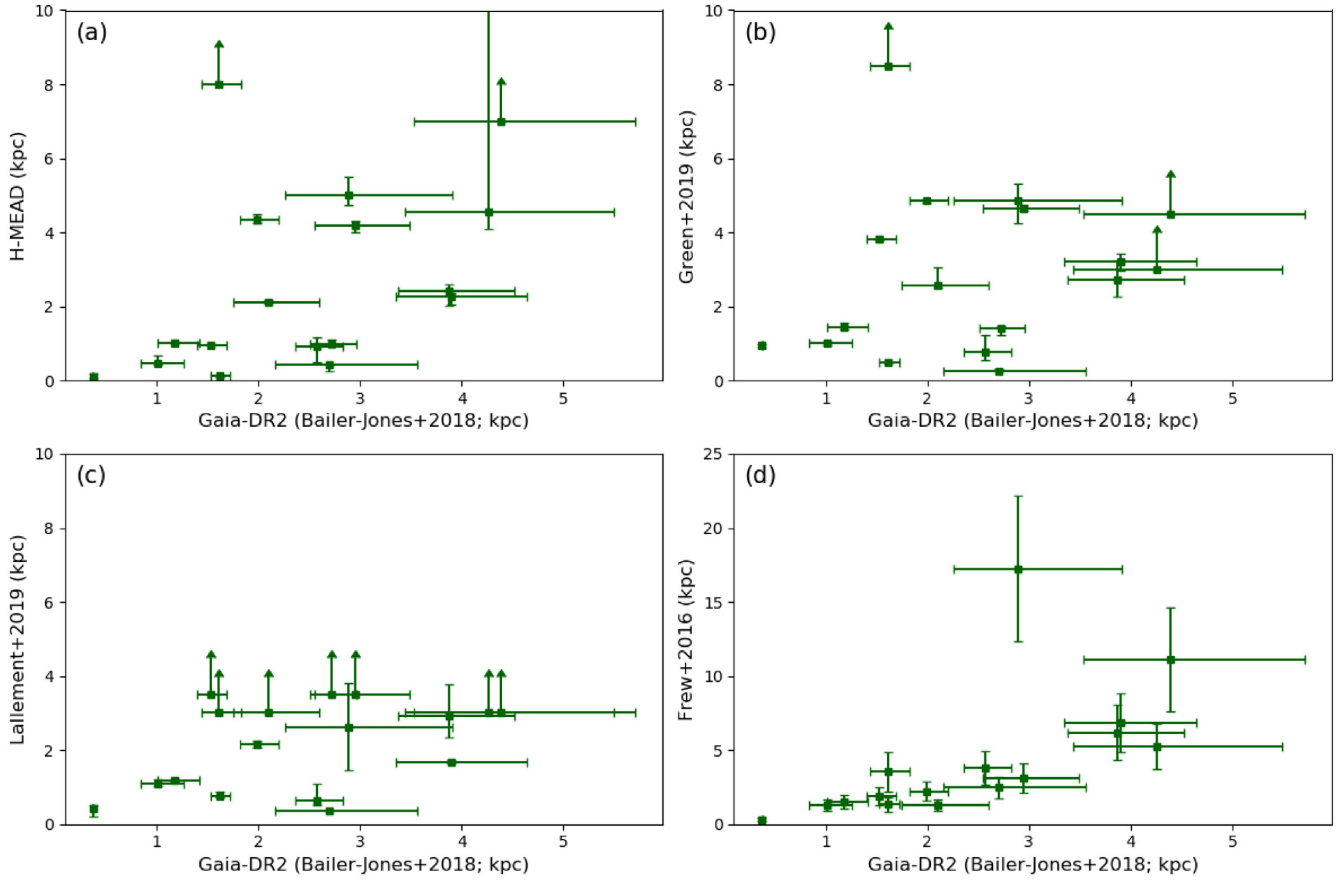

Figure 3. Correlations between *Gaia*–DR2 distances from Bailer-Jones et al. (2018) and those from the following methods. Top left-hand panel: (a) H-MEAD (Sale et al. 2014), with a Pearson correlation coefficient of $r = 0.58$ (15 PNe); top right-hand panel: (b) Green et al. (2019), with $r = 0.35$ (14 PNe); bottom left-hand panel: (c) Lallement et al. (2019), with $r = 0.57$ (10 PNe); and bottom right-hand panel: (d) Frew et al. (2016), with $r = 0.61$ (16 PNe). Upward-pointing arrows indicate lower limits, which were not used in calculating correlation coefficients. Note that the y-axis scale for plot (d) differs from those of the other three plots.

this goal, by providing 2–4 GHz radio fluxes at an angular resolution of 2.5 arcsec and with a 1σ sensitivity of 0.07 mJy by the completion of the survey.

ACKNOWLEDGEMENTS

TD's research has been supported under grants MOST104-2628-M-001-004-MY3 and MOST107-2119-M-001-031-MY3 from the Ministry of Science and Technology of Taiwan, and grant AS-IA-106-M03 from Academia Sinica. Her work was also partially funded by the Sonderforschungsbereich SFB881 'The Milky Way System' of the German Research Foundation (DFG). MB and RW acknowledge support from European Research Council grant SNDUST ERC-2015-AdG-694520. DJ and AM acknowledge support from the State Research Agency (AEI) of the Spanish Ministry of Science, Innovation and Universities (MCIU) and the European Regional Development Fund (FEDER) under grant AYA2017-83383-P.

DATA AVAILABILITY

Calibrated IPHAS images can be obtained from http://apm3.ast.cam.ac.uk/cgi-bin/wfs/dqc.cgi. H-MEAD distance-extinction data for fields within the IPHAS footprint can be obtained from http://www.iphas.org/data/extinction.

REFERENCES

Aaquist O. B., Kwok S., 1990, A&AS, 84, 229
Acker A., Stenholm B., Tylenda R., Raytchev B., 1991, A&AS, 90, 89
Acker A., Marcout J., Ochsenbein F., Stenholm B., Tylenda R., Schohn C., 1992, The Strasbourg-ESO Catalogue of Galactic Planetary Nebulae. Parts I, II
Aller L. H., Czyzak S. J., 1979, Astrophys. Space Sci., 62, 397
Bailer-Jones C. A. L., Rybizki J., Fouesneau M., Mantelet G., Andrae R., 2018, AJ, 156, 58
Barentsen G. et al., 2014, MNRAS, 444, 3230
Barker T., 1978, ApJ, 221, 145
Benedict G. F. et al., 2009, AJ, 138, 1969
Bohigas J., 2001, Rev. Mex. Astron. Astrofis., 37, 237
Cahn J. H., Rubin R. H., 1974, AJ, 79, 128
Cahn J. H., Kaler J. B., Stanghellini L., 1992, A&AS, 94, 399
Cantrell J. R., 2014, Planetary Nebulae. Available at: http://www.chara.gsu.edu/ cantrell/pne/index.htm
Capriotti E. R., Daub C. T., 1960, ApJ, 132, 677
Carrasco L., Serrano A., Costero R., 1983, Rev. Mex. Astron. Astrofis., 8, 187
Collins G. W. I., Daub C. T., O'Dell C. R., 1961, ApJ, 133, 471
Condon J. J., Kaplan D. L., 1998, ApJS, 117, 361
Corradi R. L. M. et al., 2011, MNRAS, 410, 1349
DENIS Consortium, 2003, VizieR Online Data Catalog: The DENIS database. p. B/denis
Drew J. E. et al., 2005, MNRAS, 362, 753

Frew D. J., Parker Q. A., 2010, Publ. Astron. Soc. Austr., 27, 129
Frew D. J., Bojičić I. S., Parker Q. A., 2013, MNRAS, 431, 2
Frew D. J., Parker Q. A., Bojičić I. S., 2016, MNRAS, 455, 1459
Gaia Collaboration, 2018, A&A, 616, A1
Gathier R., Pottasch S. R., Pel J. W., 1986, A&A, 157, 171
Gaustad J. E., McCullough P. R., Rosing W., Van Buren D., 2001, PASP, 113, 1326
Giammanco C. et al., 2011, A&A, 525, A58
González-Santamaría I., Manteiga M., Manchado A., Ulla A., Dafonte C., 2019, A&A, 630, A150
González-Solares E. A. et al., 2008, MNRAS, 388, 89
Green G. M. et al., 2015, ApJ, 810, 25
Green G. M., Schlafly E., Zucker C., Speagle J. S., Finkbeiner D., 2019, ApJ, 887, 93
Guerrero M. A., Manchado A., Serra-Ricart M., 1996, ApJ, 456, 651
Henry R. B. C., Kwitter K. B., Jaskot A. E., Balick B., Morrison M. A., Milingo J. B., 2010, ApJ, 724, 748
Higgs L. A., 1971, Publ. Astrophys. Branch NRC Ottawa, 1, 1
Howarth I. D., 1983, MNRAS, 203, 301
Howarth I. D., Murray J., Mills D., Berry D. S., 2004, Starlink User Note, 50
Huggins P. J., Bachiller R., Planesas P., Forveille T., Cox P., 2005, ApJS, 160, 272
Irabor T. et al., 2018, MNRAS, 480, 2423
Isaacman R., 1984, MNRAS, 208, 399
Kaler J. B., 1976, ApJS, 31, 517
Kaler J. B., 1983a, ApJ, 264, 594
Kaler J. B., 1983b, ApJ, 271, 188
Kaler J. B., Lutz J. H., 1985, PASP, 97, 700
Kaler J. B., Shaw R. A., Kwitter K. B., 1990, ApJ, 359, 392
Kaler J. B., Shaw R. A., Browning L., 1997, PASP, 109, 289
Karachentsev I. D., Karachentseva V. E., Huchtmeier W. K., 2001, A&A, 366, 428
Kerber F., Mignani R. P., Guglielmetti F., Wicenec A., 2003, A&A, 408, 1029
Kerton C. R., Brunt C. M., 2003, A&A, 399, 1083
Kimeswenger S., Barría D., 2018, A&A, 616, L2
Kwitter K. B., Henry R. B. C., 2001, ApJ, 562, 804
Kwok S., Aaquist O. B., 1993, PASP, 105, 1456
Lacy M. et al., 2020, PASP, 132, 035001
Lallement R., Vergely J. L., Valette B., Puspitarini L., Eyer L., Casagrande L., 2014, A&A, 561, A91
Lallement R., Babusiaux C., Vergely J. L., Katz D., Arenou F., Valette B., Hottier C., Capitanio L., 2019, A&A, 625, A135
Lindegren L. et al., 2018, A&A, 616, A2
Lopez J. A., Vazquez R., Rodriguez L. F., 1995, ApJ, 455, L63
Loup C., Forveille T., Omont A., Paul J. F., 1993, A&AS, 99, 291
Lumsden S. L., Hoare M. G., Urquhart J. S., Oudmaijer R. D., Davies B., Mottram J. C., Cooper H. D. B., Moore T. J. T., 2013, ApJS, 208, 11
Lutz J. H., 1973, ApJ, 181, 135
Mampaso A. et al., 2006, A&A, 458, 203
Marshall D. J., Robin A. C., Reylé C., Schultheis M., Picaud S., 2006, A&A, 453, 635
Milingo J. B., Kwitter K. B., Henry R. B. C., Souza S. P., 2010, ApJ, 711, 619
Milne D. K., 1979, A&AS, 36, 227
Milne D. K., Aller L. H., 1975, A&A, 38, 183
O'Dell C. R., 1963, ApJ, 138, 1018
Ofek E. O., Frail D. A., 2011, ApJ, 737, 45
Osterbrock D. E., Stockhausen R. E., 1960, ApJ, 131, 310
Parker Q. A. et al., 2006, MNRAS, 373, 79
Parker Q. A., Bojičić I. S., Frew D. J., 2016, J. Phys.: Conf. Ser., 728, 032008
Pazderska B. M. et al., 2009, A&A, 498, 463
Peimbert M., Torres-Peimbert S., 1971, Bol. Obs. Tonantzintla Tacubaya, 6, 21
Peña M., 2005, Rev. Mex. Astron. Astrofis., 41, 423
Perek L., 1971, Bull. Astron. Inst. Czech., 22, 103
Pollacco D. L., Bell S. A., 1997, MNRAS, 284, 32
Quireza C., Rocha-Pinto H. J., Maciel W. J., 2007, A&A, 475, 217
Raddi R., Drew J. E., Steeghs D., Wright N. J., Drake J. J., Barentsen G., Fabregat J., Sale S. E., 2015, MNRAS, 446, 274
Rosado M., Kwitter K. B., 1982, Rev. Mex. Astron. Astrofis., 5, 217
Sabin L., 2008, PhD thesis, Univ. Manchester
Sabin L., Zijlstra A. A., Wareing C., Corradi R. L. M., Mampaso A., Viironen K., Wright N. J., Parker Q. A., 2010, Publ. Astron. Soc. Austr., 27, 166
Sabin L. et al., 2013, MNRAS, 431, 279
Sabin L. et al., 2014, MNRAS, 443, 3388
Sale S. E., 2012, MNRAS, 427, 2119
Sale S. E. et al., 2009, MNRAS, 392, 497
Sale S. E. et al., 2014, MNRAS, 443, 2907
Schlafly E. F., Finkbeiner D. P., 2011, ApJ, 737, 103
Schlegel D. J., Finkbeiner D. P., Davis M., 1998, ApJ, 500, 525
Schwarz H. E., Monteiro H., 2006, ApJ, 648, 430
Setia Gunawan D. Y. A., de Bruyn A. G., van der Hucht K. A., Williams P. M., 2003, ApJS, 149, 123
Siódmiak N., Tylenda R., 2001, A&A, 373, 1032
Skiff B. A., 2014, VizieR Online Data Catalog. p. B/mk
Stanghellini L., Shaw R. A., Villaver E., 2008, ApJ, 689, 194
Storey P. J., Hummer D. G., 1995, MNRAS, 272, 41
Storey P. J., Zeippen C. J., 2000, MNRAS, 312, 813
Turatto M. et al., 1990, AJ, 99, 1170
Turner K. C., Terzian Y., 1984, AJ, 89, 501
Viironen K. et al., 2009a, A&A, 502, 113
Viironen K. et al., 2009b, A&A, 504, 291
Vink J. S., Drew J. E., Steeghs D., Wright N. J., Martin E. L., Gänsicke B. T., Greimel R., Drake J., 2008, MNRAS, 387, 308
VTech, 2014, VTSS: The Virginia Tech Spectral-Line Survey. Available at: http://www.phys.vt.edu/ halpha/
Walsh J. R., Monreal-Ibero A., Barlow M. J., Ueta T., Wesson R., Zijlstra A. A., 2016, A&A, 588, A106
Weidmann W. A., Díaz R. J., 2008, PASP, 120, 380
Zhang Y. et al., 2005, A&A, 442, 249
Zijlstra A. A., Pottasch S. R., Bignell C., 1989, A&AS, 79, 329

SUPPORTING INFORMATION

Supplementary data are available at *MNRAS* online.

APPENDIX A. IPHAS H α Flux Measurements.
APPENDIX B. Hβ and Radio Fluxes for the Sample PNE.
APPENDIX C. E(H α–H β)-Based $C_{\mathrm{H}\beta}$ and A_{v} Values.
APPENDIX D. A_{V} Values from Comparisons of Balmer-Line and Radio Fluxes.
APPENDIX E. H-MEAD Extinction Versus Distance Plots.

Please note: Oxford University Press is not responsible for the content or functionality of any supporting materials supplied by the authors. Any queries (other than missing material) should be directed to the corresponding author for the article.

This paper has been typeset from a TEX/LATEX file prepared by the author.